Dalton Transactions

ROYAL SOCIETY OF CHEMISTRY

PAPER

View Article Online
View Journal | View Issue

Cite this: *Dalton Trans.*, 2024, **53**, 17233

Spin crossover Fe^{III} complexes with a substituted Hqnal ligand: effects of anions and solvents†

Feng-Li Chen,‡ Xin-Li Liu,‡ Yue Zhao, Gang Li, Bo-Hong Gao and Xin-Yi Wang *

Received 6th July 2024,
Accepted 2nd October 2024

DOI: 10.1039/d4dt01954g

rsc.li/dalton

A new substituted Hqnal ligand, Hqnal-5-Br_q, and four resulting Fe^{III} complexes [Fe(qnal-5-Br_q)$_2$]A·sol (A = NO_3^-, sol = CH_3OH **1**; A = ClO_4^-, sol = CH_3OH **2**; A = OTf^-, sol = $2CH_3OH{\cdot}H_2O$ **3**; and A = NTf_2^-, sol = CH_2Cl_2 **4**; Hqnal-5-Br_q = *N*-(5-bromo-8-quinolinyl)-2-hydroxynaphthaldimine), have been synthesized and characterized. All four complexes, despite having different anions, adopt similar 1D [Fe(qnal-5-Br_q)$_2$]$^+$ cation chains linked by orthogonal π···π interactions. These chains are further connected to form 2D and 3D structures by other supramolecular interactions. Complexes **1–3** all exhibit abrupt spin crossover behaviors, with the transition temperatures being 230, 189, and 185 K, respectively, while complex **4** is in a high-spin state. The influence of solvents on spin crossover properties was assessed *via* magnetic measurements on the desolvated samples. Following desolvation, while complexes **1** and **2** show slight variations in their transition temperatures, complexes **3** and **4** undergo significant changes in their magnetic profiles. Desolvation in complex **3** leads to either a HS state or a very incomplete hysteretic transition with a low transition temperature for different sample batches. In contrast, the gradual desolvation in complex **4** leads to diminished solvent residues and progressive transition from a stable HS state to an SCO-active state.

Introduction

Spin crossover (SCO) materials, characterized by their magnetic bistability, have attracted much attention over the past few decades for their potential use in molecular switches, sensors, and data storage devices.[1,2] These materials, which often contain metal ions with the d^4–d^7 electron configuration, are capable of switching between low spin (LS) and high spin (HS) states under an external field.[3] Among the various SCO materials,[4] Fe^{III} complexes have been a focal point of our research due to their enhanced air stability compared to their Fe^{II} counterparts. The smaller changes in metal–ligand bond lengths and spin entropy during SCO in Fe^{III} complexes (0.10–0.13 Å and 9.13 J K^{-1} mol^{-1}) as opposed to Fe^{II} complexes (~0.20 Å and 13.38 J K^{-1} mol^{-1}) lead to different SCO characteristics.[5,6] These differences result in the challenges of achieving abrupt transitions with wide hysteresis loops around room temperature and observing the LIESST effect.[7]

In the realm of the Fe^{III} SCO materials, complexes featuring two tridentate Schiff-base ligands and an N_4O_2 coordination environment have been intensively focused on.[8,9] In this sense, Hqsal (*N*-quinolylsalicylaldimine) and its various derivatives (Scheme 1) are among the most extensively studied ligands.[9–11] Notably, the complexes [Fe(qsal)$_2$]NCSe·sol (sol = MeOH, CH_2Cl_2, and DMSO) exhibit remarkably wide hysteresis loops (115–180 K for the initial cycle and 70–76 K for the subsequent cycles).[12,13] This strong cooperativity is attributed to the effective π···π interactions between the qsal ligands. These results, along with subsequent multifunctional materials containing the [Fe(qsal)$_2$]$^+$ units and redox-active anions, have prompted a deeper investigation of SCO complexes with the Hqsal ligand and its various derivatives, Hqsal-*n*-R ('*n*' denotes the position of the substituent on the benzene (Ph) ring, and 'R' represents different substituents).[14–17] These studies have demonstrated the efficient modification of the ligand field and cooperativity by the ligand substituents that resulted in a variety of intriguing SCO behaviors and the establishment of detailed magneto-structural relationships. Halogen-substituted Hqsal ligands, for instance, have been extensively studied, with [Fe(qsal-5-X)$_2$]NTf_2 (X = Cl, Br, I) showing distinct SCO behaviors.[18] Notably, [Fe(qsal-5-I)$_2$]NTf_2 exhibits an abrupt hysteresis loop of approximately 34 K, indicating a stronger coop-

State Key Laboratory of Coordination Chemistry, Collaborative Innovation Center of Advanced Microstructures, School of Chemistry and Chemical Engineering, Nanjing University, Nanjing, 210023, China. E-mail: wangxy66@nju.edu.cn

†Electronic supplementary information (ESI) available: Physical measurement details, structure information in detail, powder XRD spectra, and additional magnetic figures. CCDC 2367591–2367599 and 2384171. For ESI and crystallographic data in CIF or other electronic format see DOI: https://doi.org/10.1039/d4dt01954g

‡These authors contributed equally.

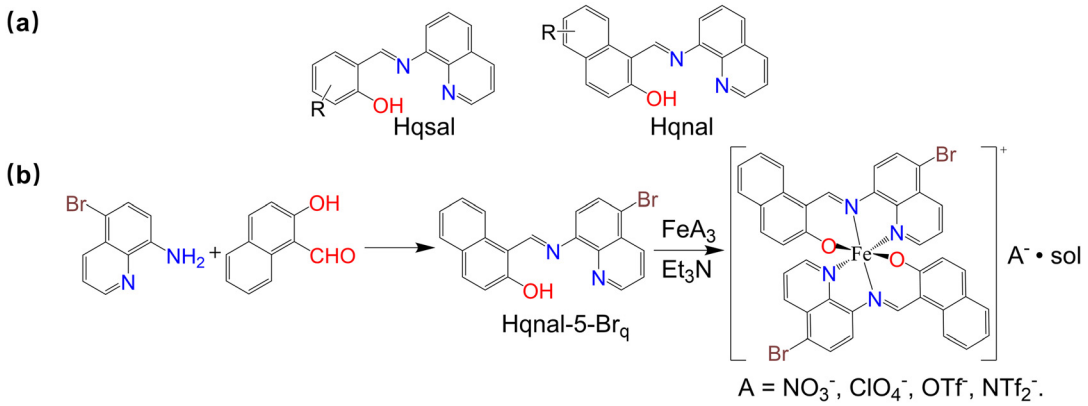

Scheme 1 (a) The structures of the Schiff-base ligands Hqsal-*n*-R and Hqnal-*n*-R; (b) the synthesis of the Hqnal-5-Br$_q$ ligand and [Fe(qnal-5-Br$_q$)$_2$]A·solvent complexes.

erative effect as one moves from Cl to I. Furthermore, the influence of lattice solvents and charge-balancing anions on the structures and the resulting SCO performances has been nicely illustrated in complexes such as [Fe(qsal-5-Cl)$_2$]NO$_3$·sol (sol = MeOH, EtOH, and i-PrOH),[19] [Fe(qsal-5-I)$_2$]A·sol (A = OTf$^-$, NTf$_2^-$, sol = MeOH, EtOH, *n*-PrOH, i-PrOH, MeCN, and acetone),[20] [Fe(qsal-4-F)$_2$]A·sol (A = NO$_3^-$, sol = 0.91MeOH·0.57H$_2$O; PF$_6^-$; BF$_4^-$; OTf$^-$, sol = 1.5MeOH),[21] and [Fe(qsal-5-F)$_2$]A (A = NO$_3^-$, PF$_6^-$, BF$_4^-$, ClO$_4^-$, SCN$^-$),[22] respectively.

As previously highlighted, robust π···π interactions can effectively increase cooperativity and thereby enhance the SCO performance. To further enhance these interactions, a novel tridentate Schiff-base ligand with an expanded π system, namely Hqnal (*N*-(8-quinolinyl)-2-hydroxy-1-naphthaldimine) (Scheme 1a), was designed and employed to prepare new Fe^{III} SCO complexes. Interesting properties, such as the abrupt transition with a 31 K hysteresis loop observed in [Fe(qnal)$_2$]NS[23] and the modulation of conductivity in the SCO conducting molecular compound [Fe(qnal)$_2$][Pd(dmit)$_2$]$_5$·acetone,[24] were observed. However, in contrast to the extensively studied Hqsal-*n*-R complexes, investigations into Hqnal derivatives have been notably sparse. To our knowledge, only one known example of a Hqnal derivative, 7-methoxy-1[(8-quinolinylimino)methyl]-2-naphthaleno (Hqnal-7-OMe) featuring an OMe substituent group, has been reported. From this ligand, two complexes, [Fe(qnal-7-OMe)$_2$]PF$_6$·acetone and [Fe(qnal-7-OMe)$_2$]BPh$_4$·2MeOH, were prepared.[25] Remarkably, the MeOH solvated complex displayed an exceptionally wide hysteresis loop of 110 K.

Considering the success of Hqsal derivatives in Fe^{III} SCO complexes, we are optimistic that employing similar strategies with Hqnal ligands bearing various substituents will lead to the discovery of new Fe^{III} SCO complexes with interesting properties. In line with this, we have recently reported the first quinoline-substituted Hqsal ligand, Hqsal-5-Br$_q$ ("q" specifies that the substitution occurs on the quinoline ring), and a series of Fe^{III} complexes, [Fe(qsal-5-Br$_q$)$_2$]A·CH$_3$OH (A = NO$_3^-$, BF$_4^-$, PF$_6^-$, and OTf$^-$). Both complexes with NO$_3^-$ and BF$_4^-$ anions exhibit abrupt SCO transitions with a 5 K hysteresis loop.[26]

Following this recent work, we now present our research on the quinoline-substituted Hqnal ligand. To date, apart from the previously mentioned Hqnal-7-OMe ligand, no other Hqnal derivatives have been reported. By introducing a Br atom into the quinoline group, we designed a new ligand, *N*-(5-bromo-8-quinolinyl)-2-hydroxynaphthaldimine (Hqnal-5-Br$_q$, Scheme 1b). The incorporation of the Br atom into the quinoline group is expected to modulate the ligand field strength of the Hqnal ligand. Moreover, the presence of the Br atom could also engender various weak interactions, such as halogen bond, C–H···Br hydrogen bond, and Br···π interactions. These interactions have the potential to strengthen the cooperative effects within the system, thereby enhancing the SCO properties. Utilizing this ligand, we have synthesized a series of new complexes, [Fe(qnal-5-Br$_q$)$_2$]A·sol (A = NO$_3^-$ **1**, ClO$_4^-$ **2**, OTf$^-$ **3**, and NTf$_2^-$ **4**). These complexes have been structurally and magnetically analyzed, providing valuable insights into the impact of the quinoline substitution of the Hqnal ligand and the anions on the SCO properties of Fe^{III} complexes. Furthermore, the impact of the crystallized solvents on the SCO properties of all complexes has been examined. Specifically, complexes **3** and **4** show pronounced changes in SCO properties upon desolvation, occurring through a precise crystal-to-crystal transition for complex **3** and a more gradual desolvation process for complex **4**. These complexes represent the first Fe^{III} SCO complexes featuring a quinoline-substituted Hqnal ligand.

Experimental section

Materials

All experiments were conducted under aerobic conditions, utilizing chromatographic-grade solvents for the synthesis. All

chemicals were purchased from Energy Chemicals or Bidepharm and used as received without further purification.

Caution! Although we experienced no issues during our experiments, perchlorate salts are potentially explosive and should be used in small quantities and handled with care.

Physical measurements

Comprehensive characterization of the ligand and complexes was performed using various techniques. Powder X-ray diffraction (PXRD) data were obtained using a Bruker D8 Advance diffractometer with a Cu Kα X-ray source (λ = 1.54056 Å) at 40 mA and 40 kV, scanning over a 2θ range of 5–50°. UV–vis spectra were recorded using a UV-1900 UV–visible spectrophotometer (SHIMADZU, Japan) for **1–4** and **3·0.6H_2O** in CH_2Cl_2. Bruker AVANCE III 600 MHz spectrometers were used to measure the ^{1}H and ^{13}C NMR spectra, with tetramethylsilane (TMS) as the internal standard. FT-IR absorption spectra were measured using a Bruker Vertex 70 V spectrometer (Germany) in the range of 4000–400 cm^{-1} at room temperature. The ATR measurements were conducted with a Platinum-ATR accessory equipped with a pure diamond crystal. Thermogravimetric analysis (TGA) was performed on a PerkinElmer Thermal Analyzer in the temperature range of 30–600 °C in Al_2O_3 crucibles at a heating rate of 10 °C min^{-1} under a nitrogen flow. Elemental analysis for C, H, and N was performed on an Elementar Vario MICRO analyzer. Differential scanning calorimetry (DSC) was performed on a METTLER-DSC1 instrument, with a cooling/warming rate of 5 K min^{-1} under nitrogen. Magnetic measurements for all complexes were carried out using a Quantum Design VSM magnetometer, under a direct current (dc) field of 1000 Oe between 5 K and 300 K or up to 400 K at a cooling/heating rate of 5 K min^{-1}. The experimental data were corrected for the diamagnetic contributions from both the sample holders and the complexes using Pascal's constants.

X-ray crystallography

Single crystal X-ray diffraction data were obtained on a Bruker APEX-II diffractometer equipped with a CCD area detector using either Mo Kα radiation (λ = 0.71073 Å) or a liquid-metal-jet X-ray source (Ga-Kα radiation, λ = 1.34139 Å) at varying temperatures. Bruker APEX-IV software was used for data collection, reduction, and absorption correction. Crystals **1** and **2**, identified as twin crystals, were analyzed using CELL_NOW[27] to determine the twin matrices, with data scaling performed by TWINABS.[28] The structures were solved and refined using the SHELXTL crystallographic software package[29,30] and OLEX2[31] by the full-matrix least-squares method on F^2. All non-hydrogen atoms were refined anisotropically, while hydrogen atoms were added based on theoretical calculations. The details of the structural refinement and data collection parameters are listed in Tables S1–S3.† Selected bond lengths are listed in Tables S4 and S5.† The distances of the supramolecular interactions, including those of hydrogen bonds (C–H···O/F/Br), halogen···π (F/Br···π), halogen bonds (Br···O), C–H···π, and π···π interactions, are listed in Tables S6–S10.† The CCDC numbers are 2367591–2367599 and 2384171.

Synthesis of *N*-(5-bromo-8-quinolinyl)-2-hydroxynaphthaldimine (Hqnal-5-Br$_q$). The ligand Hqnal-5-Br$_q$ was synthesized following a literature procedure.[32] Specifically, 5-bromoquinolin-8-amine (5 mmol, 1.1154 g) and 2-hydroxy-1-naphthaldehyde (5.5 mmol, 0.9470 g) were combined in absolute ethanol (about 50 ml) in a round-bottomed flask. The mixture was heated under reflux overnight, resulting in the formation of orange microcrystals. The microcrystals were then collected *via* vacuum filtration, washed with diethyl ether, and air-dried. To obtain a single crystal suitable for X-ray diffraction, the orange microcrystals were dissolved in dichloromethane and allowed to evaporate slowly in a refrigerator for two weeks. Yield: 1.1544 g, 61.2%. Elemental analysis: calcd (%) for $C_{20}H_{13}BrN_2O$ (377.24 g mol^{-1}): C 63.67, N 7.43, H 3.47; found C 63.71, N 7.38, H 3.51. Selected FT-IR data (cm^{-1}): 3025, 2944 (ν_{C-H}), and 1622 ($\nu_{C=N}$). The ^{1}H and ^{13}C NMR (600 MHz, DMSO-d_6) of the ligand can be found in Fig. S1 and S2.†

Synthesis of [Fe(qnal-5-Br$_q$)$_2$]NO$_3$·CH$_3$OH (1). Single crystals of complex **1** were synthesized *via* the liquid phase diffusion method from the ligand and metal salt within a test tube. Hqnal-5-Br$_q$ (37.24 mg, 0.1 mmol) was dissolved in 8 mL of dichloromethane, to which Et_3N (14 μL) was added. After stirring for 30 minutes, the light orange solution was filtered and transferred to the bottom of a 20 mL test tube. Concurrently, $Fe(NO_3)_3·9H_2O$ (0.0202 g, 0.05 mmol) was dissolved in 7 mL of methanol and stirred for 30 minutes. A buffer layer of a mixture of methanol and dichloromethane (1 : 1, 4 mL) was carefully layered on top of the ligand solution. Finally, the metal salt solution was layered on top of the buffer layer. The test tube was left undisturbed at room temperature. Black plate-like single crystals suitable for X-ray analysis were obtained in about ten days. The crystals were collected, washed with methanol, and air-dried at room temperature. Yield: 0.0233 g, 51.6% (based on Fe). Elemental analysis: calcd (%) for $C_{41}H_{28}Br_2FeN_5O_6$ (902.33 g mol^{-1}): C 54.57, N 7.76, H 3.13; found C 54.66, N 7.53, H 3.21. Selected FT-IR data (cm^{-1}): 3363 (ν_{O-H}), 3022, 2979 (ν_{C-H}), 1603 ($\nu_{C=N}$), 1374, and 1339 ($\nu_{N=O}$).

Synthesis of [Fe(qnal-5-Br$_q$)$_2$]ClO$_4$·CH$_3$OH (2), [Fe(qnal-5-Br$_q$)$_2$]OTf·2CH$_3$OH·H$_2$O (3), and [Fe(qnal-5-Br$_q$)$_2$]NTf$_2$·CH$_2$Cl$_2$ (4). Following a similar process to that for complex **1**, complexes **2–4** were synthesized using $Fe(ClO_4)_3·xH_2O$ (0.0177 g, 0.05 mmol), $Fe(OTf)_3$ (0.0252 g, 0.05 mmol), or $FeCl_3·6H_2O$ (0.0135 g, 0.05 mmol) and $LiNTf_2$ (0.0431 g, 0.15 mmol) as the metal salts. Black single crystals (needle-like for **2** and **4** and rhomboid for **3**) were obtained in about fifteen days. Yield: 0.0250 g, 53.2% (**2**), 0.0278 g, 53.5% (**3**), and 0.0331 g, 56.4% (**4**) (based on Fe). Elemental analysis: calcd (%) for **2** ($C_{41}H_{28}Br_2ClFeN_4O_7$, 939.79 g mol^{-1}): C 52.40, N 5.96, H 3.00; found C 52.79, N 6.05, H 2.79; **3** ($C_{43}H_{34}Br_2F_3FeN_4O_8S$, 1039.45 g mol^{-1}): C 49.68, N 5.39, H 3.30; found C 49.76, N 5.39, H 3.35; **4** ($C_{43}H_{26}Br_2Cl_2F_6FeN_5O_6S_2$, 1173.36 g mol^{-1}): C 44.01, N 5.97, H 2.23; found C 44.19, N 5.95, H 2.31. Selected FT-IR data (cm^{-1}) for **2**: 3031, 2977 (ν_{C-H}), 1616

($\nu_{C=N}$), 1076 ($\nu_{Cl=O}$), 621 (ν_{Cl-O}); **3**: 3478 (ν_{O-H}), 3054, 2944 (ν_{C-H}), 1588 ($\nu_{O=H}$), 1254, 1028 (ν_{S-O}), 1146 (ν_{C-F}); **4**: 3058, 2981 (ν_{C-H}), 1603 ($\nu_{C=N}$), 1335, 1134 ($\nu_{S=O}$), 1190 (ν_{C-F}). It is noteworthy that crystals of **2** are prone to losing solvent, and the elemental analysis is in good agreement with that of the desolvated crystal. This was also proved by other characterization techniques.

Synthesis of [Fe(qnal-5-Br$_q$)$_2$]OTf·0.6H$_2$O (3·0.6H$_2$O). The desolvated crystals of complex **3**, referred to as **3·0.6H$_2$O**, were prepared by drying complex **3** at 140 °C in a vacuum oven for 24 h. Elemental analysis: calcd (%) for $C_{41}H_{25.2}Br_2F_3FeN_4O_{5.6}S$ (968.17 g mol^{-1}): C 50.86, N 5.79, H 2.62; found C 50.79, N 5.85, H 2.57. Selected FT-IR data (cm^{-1}): 3478 (ν_{O-H}), 3054, 2944 (ν_{C-H}), 1588 ($\nu_{O=H}$), 1254, 1028 (ν_{S-O}), 1146 (ν_{C-F}).

The phase purity of these complexes was confirmed through PXRD experiments on freshly prepared samples (Fig. S3†). For complexes **1**, **3**, and **4**, the experimental diffraction patterns closely matched the simulated patterns derived from single crystal data. However, complex **2** showed a slight discrepancy in peak intensities, likely attributed to crystal orientation effects. In addition, the numbers of the lattice solvent molecules were validated by the thermogravimetric analysis (TGA) of all five complexes (Fig. S4†). The weight losses over specific temperature ranges are 3.48% (30–278 °C), 3.43% (20–195 °C), 7.72% (30–205 °C), 7.31% (30–140 °C), and 1.45% (30–100 °C) for complexes **1–4** and **3·0.6H$_2$O**, respectively. These weight losses are in agreement with the elemental analysis results and single crystal structure data. Furthermore, the TGA data indicate that the crystallized solvents are prone to loss, highlighting the necessity of using freshly prepared samples for other measurements. We have also measured the UV-visible spectra of complexes **1–4** and **3·0.6H$_2$O** in CH_2Cl_2. As shown in Fig. S5,† similar absorption curves were observed for these complexes, with peaks in about 350 nm and 450 nm assigned to the π–π* and ligand-to-metal charge-transfer (LMCT) transitions, respectively.[33]

Results and discussion

Crystal structure

The ligand Hqnal-5-Br$_q$ was prepared *via* Schiff-base condensation, resulting in a microcrystalline form. Its asymmetric unit is depicted in Fig. S6,† with the crystal parameters listed in Table S3.† A PXRD study (Fig. S3e†) confirms the high purity of the ligand Hqnal-5-Br$_q$. We will not discuss the ligand in detail.

To obtain the structures of both spin states, the crystal data for the complexes were collected at different temperatures (100 and 300 K for complexes **1**, **3**, and **4**, and 90 K for complex **2**). Our attempts to obtain the high-spin state structure of complex **2** at high temperature were unsuccessful due to the loss of crystallinity. Despite variations in counterions and lattice solvents, complexes **1–4** and **3·0.6H$_2$O** all crystallized in the triclinic crystal system with the $P\bar{1}$ space group. The asymmetric units for complexes **1–4** are displayed in Fig. 1. For all

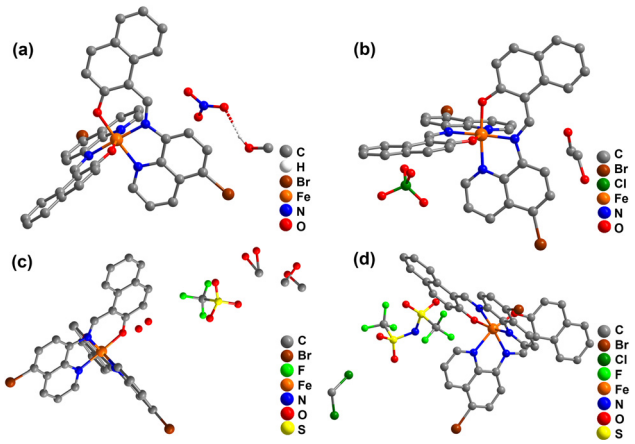

Fig. 1 The asymmetric units of **1** (a), **2** (b), **3**(c), and **4** (d).

of them, the asymmetric units consist of a [Fe(qnal-5-Br$_q$)$_2$]$^+$ cation, a charge-balancing anion (NO_3^-, ClO_4^-, OTf^-, and NTf_2^-), and some lattice solvent molecules (one ordered MeOH molecule for **1**, one disordered MeOH for **2**, one disordered water and two disordered MeOH molecules for **3**, and a CH_2Cl_2 molecule for **4**, respectively). For desolvated **3·0.6H$_2$O**, there is still 0.6 water molecule in the asymmetric unit, and the OTf^- anion displays serious disorder. Efforts to obtain a completely desolvated crystal of **3** and the desolvated crystal structures of the other complexes were unsuccessful. As observed in other similar complexes from Hqsal-*n*-R and Hqnal ligands,[34–37] complexes **1–4** all feature Fe^{III} centers coordinated by two tridentate Hqnal-5-Br$_q$ ligands. These two ligands are nearly perpendicular to one another in a meridional arrangement, forming a pseudo-octahedral N_4O_2 coordination sphere with the oxygen atoms of Hqnal-5-Br$_q$ positioned in a *cis*-position.

Crystal data of these complexes correlate well with the magnetic measurements, illustrating the differences between the HS and LS states of the complexes. A key indicator of the spin state change is the average coordination bond length (Fe–O$_{av}$ and Fe–N$_{av}$). At low temperatures, the average bond lengths of Fe–O$_{av}$ and Fe–N$_{av}$ for complexes **1**, **2**, and **3** are indicative of an LS state,[9,11,36] with values of 1.878 Å and 1.954 Å for **1**, 1.880 Å and 1.954 Å for **2**, and 1.876 Å and 1.960 Å for **3**, respectively (Tables S4 and S5†). In contrast, at higher temperatures, complexes **1** and **3** exhibit average bond lengths of 1.920 Å and 2.114 Å, and 1.906 Å and 2.116 Å, aligning with those expected for HS Fe^{III} complexes.[37,38] For the desolvated complex **3·0.6H$_2$O**, the bond lengths of Fe–O$_{av}$ and Fe–N$_{av}$ are 1.921 Å and 2.126 Å at 150 K (Table S4†), indicating that it remains in the HS state at this temperature. Complex **4**, however, maintains HS state bond lengths at both low and high temperatures. The changes in bond lengths (ΔFe–O$_{av}$ and ΔFe–N$_{av}$) for complexes **1** and **3** are 0.03 Å and 0.160 Å, and 0.03 Å and 0.156 Å, respectively. For complex **4**, these changes are minimal (0.0099 Å and 0.012 Å), indicating no significant spin state change. Furthermore, octahedral distortion para-

meters (Θ, Σ) are valuable for assessing the spin state, with an HS state corresponding to greater distortion and an LS state to a more regular octahedron.[37] The complexes exhibit Σ values of 31°–36° for the LS state and 68°–75° for the HS state, and Θ values of 92°–110° and 249°–282°, respectively (Tables S4 and S5†). Changes in these distortion parameters ($\Delta\Sigma$ and $\Delta\Theta$) confirm the extent of SCO.[39] These distortion parameters are also consistent with the CShM (continuous shape measures) parameters calculated using Shape 2.1[40] (Tables S4 and S5†), where higher values indicate greater octahedral distortion. In addition, the unit cell volume for complexes **1** and **3** changes by approximately 60 Å^3 between the LS and HS states, a change previously observed in other Fe^{III} SCO complexes.[11]

Crystal packing of the complexes

It is widely accepted that enhancing intermolecular cooperativity is key to achieving SCO complexes with abrupt near-room-temperature transitions and wide hysteresis loops. To delve into these interactions and the resulting cooperativity, the supramolecular interactions involving $[Fe(qnal\text{-}5\text{-}Br_q)_2]^+$ cations and the crystal packing of the complexes were carefully examined.

Similar to some reported $[Fe(qsal\text{-}n\text{-}R)_2]^+$ complexes with the "chain-layers" structures,[21,26] $[Fe(qnal\text{-}5\text{-}Br_q)_2]^+$ cations in complex **1** are interconnected by two sets of orthogonal π···π interactions between the naphthalene ring and quinoline ring, forming a 1D chain along the *c* axis (Fig. 2). These interactions are denoted as type A (with center–center distances of 3.691 Å and 3.785 Å) and type B (with center–center distances of 3.876 Å, 3.682 Å, and 3.638 Å) (Fig. 2b and Table S6†). In addition to these π···π interactions, $[Fe(qnal\text{-}5\text{-}Br_q)_2]^+$ cations within the chain are further linked by C–H···O hydrogen bonds at approximately 2.6 Å–2.8 Å and by weak C–H···Br interactions at about 3.4 Å–3.6 Å (Fig. 2 and Table S6†). The cross-section of the 1D chain is nearly square (Fig. 2a), indicating nearly equal Fe–Fe distances in the type A and type B π···π interactions (ΔFe–Fe = 0.08 Å). The presence of this kind of a 1D chain structure is indicative of SCO behavior, as previously observed in $[Fe(qsal\text{-}n\text{-}R)_2]^+$ complexes.[21,22,26,41] In addition, the NO_3^- anion employs non-classical hydrogen bonds[20] (C–H···O at distances of about 2.4 Å–2.9 Å) to connect adjacent cations, further enhancing intrachain interactions (Fig. 2c and Table S6†). However, no interactions are observed between $[Fe(qnal\text{-}5\text{-}Br_q)_2]^+$ cations and methanol molecules within the 1D chains. At high temperatures, most supramolecular interactions weaken with increased bond distances, such as increases of 0.181 Å for type A and 0.101 Å for type B π···π interactions, and about 0.1 Å for C–H···O bonds (Table S6†). Additionally, it is noted that NO_3^- anion is disordered at 300 K and well-ordered at 100 K, likely due to the structure becoming more flexible at elevated temperatures.

Adjacent 1D chains in complex **1** are interconnected through weak interactions among cations, anions, and solvent molecules, assembling into 2D layers within the *ac* plane. Specifically, π···π interactions between the naphthalene rings of adjacent cations (type C) and C–H···O hydrogen bonds between cations and anions and solvent MeOH molecules, contribute to the formation of the 2D network (Fig. 3 and S7†). These layers are then linked by additional weak interactions, such as C–H···Br and Br···π involving the cations, and C–H···O and Br···O interactions involving MeOH molecules and NO_3^- anions, to construct the complete 3D structure (Fig. S7†). At high temperatures, certain interactions become weaker or even disappear (Table S6†). The lattice solvents and anions are located within the cavities of the chains and layers. Moreover, the distance between neighboring chains (d_{chain}) and layers (d_{layer}), as shown in Fig. 4a, also changes at different temperatures. Notably, at low temperatures, d_{chain} is 11.35 Å and d_{layer} is 12.60 Å, which is 0.30 Å shorter than d_{chain} and 0.33 Å longer than d_{layer} at high temperatures, respectively. This correlates with the longer *b* axis value in the LS state compared to the HS state (Table S1†), suggesting that the more tightly packed chains at lower temperatures result in the separation of the 2D layers.

Given their isostructural nature, the packing structure of complex **2** mirrors that of complex **1**, and comprises similar 1D chains with a square cross-section (Fig. S8a†) formed by π···π interactions of types A and B (Fig. S9b†) and the 2D and 3D structures connected by other weak interactions (Fig. S10 and S11a†). However, the presence of different anions and the disorder of the MeOH molecules in **2** introduce subtle differ-

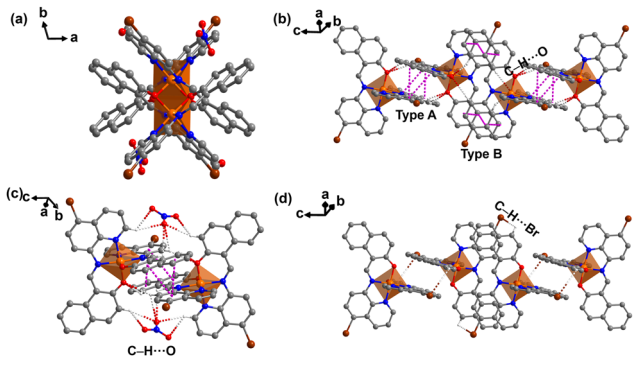

Fig. 2 The 1D chain of **1**: (a) cross-section of the 1D chain; (b) type A and type B π···π interactions and the C–H···O interactions; (c) the C–H···O interactions between NO_3^- anions and cations; and (d) the C–H···Br interactions between cations.

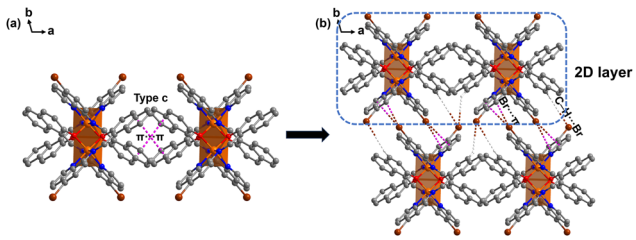

Fig. 3 (a) The 2D layer of complex **1** formed by the 1D chains connected by type C π···π interactions and (b) 3D structure of **1** formed by the 2D layers connected by C–H···Br and Br···π interactions.

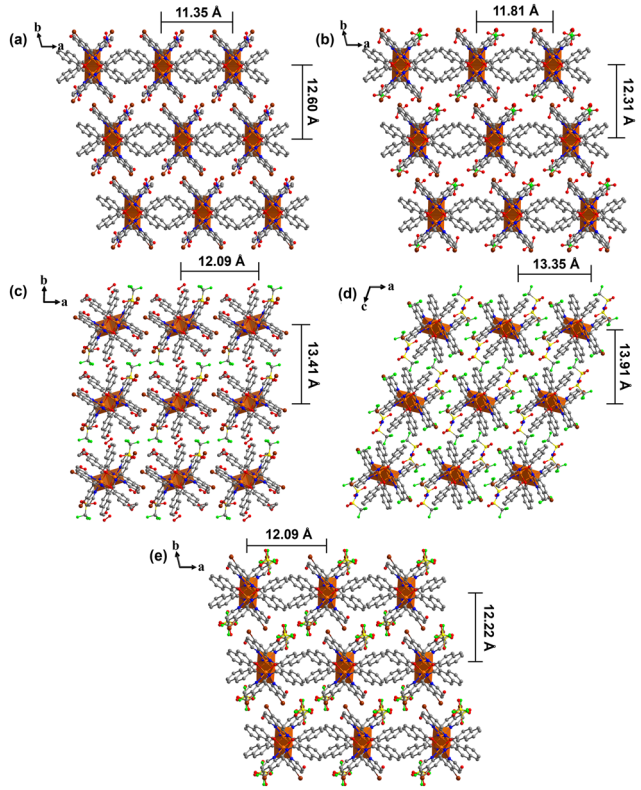

Fig. 4 The packing structures of complexes **1–4** (a–d) at the low spin state and **3·0.6H$_2$O** (e) at 150 K showing the d_{chain} and d_{layer} values.

ences in the weak interactions (Fig. S10 and Table S7†). Compared with complex **1**, the center–center distances of π···π interactions are longer in complex **2**, and there are fewer C–H···O hydrogen bonds. Furthermore, weaker and fewer supramolecular interactions between the 1D chains are observed in **2**. For instance, while C–H···O interactions involving anions and solvents were observed to connect the 1D chains to the 2D layer, the absence of type C π···π interactions is notable. Finally, the d_{chain} for **2** is found to be 0.46 Å longer, while the d_{layer} is 0.29 Å shorter than in complex **1** (Fig. 4b). These differences indicate a looser packing structure and weaker cooperativity within complex **2**.

Complex **3**, despite featuring a similar 1D chain structure as complexes **1** and **2** (Fig. S12†), exhibits obvious variations in its packing structure due to the different anions and solvents. The most significant distinction lies in the fact that in complex **3**, there are no apparent π–π interactions between the 1D chains. Instead, they are interconnected through C–H···O/Br/π and Br···π interactions to form the 2D layer (Fig. S11b†), which are further connected by other weak interactions to form the 3D structure. The intermolecular interactions, including the π···π stacking and C–H···O/Br/F interactions between the cations and the OTf$^-$ anions and MeOH solvents, are comparatively weaker than those in complexes **1** and **2** (Table S8†). However, despite their reduced strength, the number of the weak C–H···O/Br/F interactions surpasses those in complexes **1** and **2**, leading to more or less similar intermolecular interactions between the Fe^{III} cations in these complexes. Furthermore, complex **3** exhibits longer d_{chain} and d_{layer} values compared to complexes **1** and **2** (Fig. 4c), correlating with the larger size of the OTf$^-$ anions and number of lattice solvent molecules.

Interestingly, the single crystal of **3** retains its integrity even after the removal of methanol molecules, facilitating the successful determination of the structure of **3·0.6H$_2$O** (Fig. 5). Upon this crystal-to-crystal desolvation, the unit cell parameters of **3·0.6H$_2$O** undergo significant change to become isostructural with complexes **1** and **2**. Consequently, the structure of **3·0.6H$_2$O** exhibits a remarkable resemblance to the structures of complexes **1** and **2**. Compared to complex **3**, the intrachain π···π interactions between the cations in **3·0.6H$_2$O** are slightly weaker (Fig. S11d, S13 and Table S9†). The previously well-ordered OTf$^-$ anions in complex **3** become significantly disordered over two positions in **3·0.6H$_2$O**, indicating also a relative weakening of the supramolecular interactions involving the anions. Because of the absence of methanol molecules, the original interactions between the lattice solvents and the cations, as seen in complex **3**, are no longer observed. Furthermore, the removal of MeOH molecules results in a similar 2D layer as those in complexes **1** and **2** and a tighter packing structure, reflected in the shorter d_{chain} and d_{layer} values as compared to complex **3** (Fig. 4e). While the d_{chain} value of **3·0.6H$_2$O** is larger than those of complexes **1** and **2**, the d_{layer} is slightly shorter. Due to the absence of solvent-mediated interactions and the overall weaker interactions between the cations and anions, the supramolecular interactions in **3·0.6H$_2$O** are generally weaker than those in complex **3**.

As for complex **4** with the largest NTf$_2^-$ anion, similar 1D chains are formed through a comparable set of supramolecular interactions as seen in other complexes. These interactions include type A and B π···π stacking, C–H···O/Br, and Br···π interactions (Fig. S14†). The arrangement of the 1D chains in complex **4** is similar to that of complex **3**, with no notable interchain π···π interactions between the cations. Instead, the formation of the 2D and 3D structures is facilitated by a variety of other supramolecular interactions (Fig. S11c†). The supramolecular interactions in complex **4** are generally weaker than those in the other three complexes (Table S10†). In addition, the Fe–Fe distance between the Fe^{III} centers in the 1D chain is

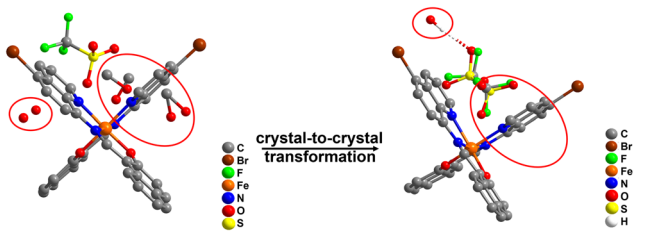

Fig. 5 The asymmetric units of complex **3** and **3·0.6H$_2$O**, showing the crystal-to-crystal desolvation.

longer than other complexes, and the 1D cross-section of the chain is rectangular, not square (Fig. S8c†), with a ΔFe–Fe distance of 0.666 Å (Table S10†). The d_{chain} and d_{layer} values are also significantly larger than those in the other complexes (Fig. 4d), indicating a more loosely packed structure, which is consistent with its HS state (*vide post*).

To analyze the intricate supramolecular interactions, Hirshfeld surface analysis, conducted using CrystalExplorer17,[42] was employed for these complexes with their low-temperature structures. The analysis revealed numerous red spots on the Hirshfeld surfaces, indicative of various supramolecular interactions including O···H, C···H, Br···H, H···H, C···C, and so on (Fig. S15†). The specific proportions of these interactions are shown in Fig. 6 and Table S11,† with 2D fingerprint plots displayed in Fig. S16† for each complex. Notably, O···H/H···O and H···H/H···H interactions predominate, indicating their significant role in the packing structures of the complexes (Fig. S17†). The intensity and proportion of these interactions are comparatively higher in complexes **1** and **2**, suggesting stronger intermolecular interactions, likely attributed to the effective involvement of NO_3^- and ClO_4^- anions. In contrast, these interactions are less pronounced and weaker in complex **3** with the larger OTf^- anion, and even more so in complex **4** containing the largest NTf_2^- anion. This reduction in interaction strength in complex **4** correlates with its looser packing and the lack of an SCO transition (*vide* post). Furthermore, the desolvation effect on complex **3** is evident, with the O···H/H···O and H···H/H···H interactions being less frequent and weaker in the desolvated **3·0.6H$_2$O** compared to complex **3** (Fig. S17†). This reduction in interaction strength aligns with the high spin state observed in **3·0.6H$_2$O** (*vide infra*).

Magnetic properties

To investigate their SCO properties, the magnetic susceptibilities of the freshly prepared crystals were measured over a temperature range of 5 to 300 K with a temperature sweep rate of 5 K min^{-1}. Furthermore, to examine the desolvation effect, the magnetic data from 5 to 400 K were also collected on the *in situ* desolvated samples, which were prepared by heating to 400 K in a SQUID VSM chamber.

Complexes **1–3** exhibited similar abrupt SCO transitions, each with slightly different transition temperatures. For complex **1** (Fig. 7a), the $\chi_M T$ value at 300 K is 4.28 cm^3 mol^{-1} K, close to the spin-only value of 4.38 cm^3 mol^{-1} K for an HS Fe^{III} ion. Upon cooling, the $\chi_M T$ curve gradually decreases to

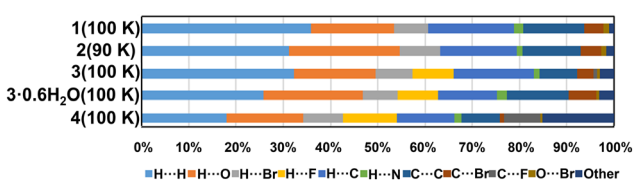

Fig. 6 Percentage contributions of supramolecular interactions for compounds **1–4** at low temperatures and **3·0.6H$_2$O** at 150 K.

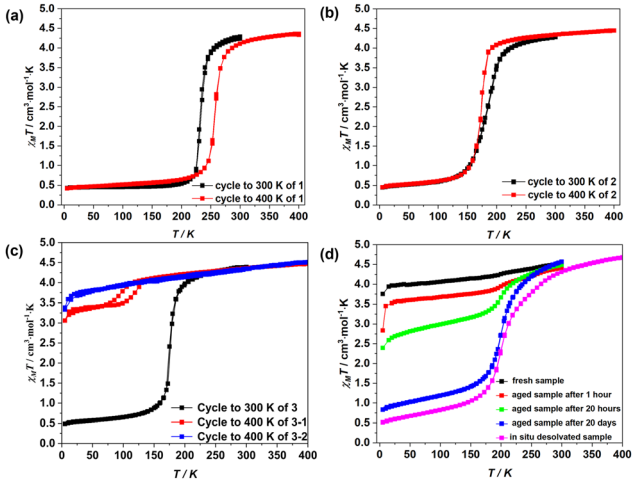

Fig. 7 $\chi_M T$ *versus* T plots for complexes **1–4** (a)–(d) in the temperature ranges of 5–300 K and 5–400 K at a cooling and heating rate of 5 K min^{-1}. The *in situ* desolvation of two batches of sample **3** leads to slightly different results, and different SCO properties were observed for complex **4** stored at room temperature for varying periods.

3.98 cm^3 mol^{-1} K at 255 K, where the majority of Fe^{III} centers remain in the HS state. An abrupt decrease of the $\chi_M T$ curve is observed upon further cooling, reaching 0.54 cm^3 mol^{-1} K at 200 K. This drop signifies an abrupt SCO in complex **1**, with an estimated transition temperature $T_{1/2}$ of 230 K, derived from the peak temperature of d($\chi_M T$)/dT. Further cooling leads to a slow decrease of $\chi_M T$ to 0.44 cm^3 mol^{-1} K at 5 K, which is slightly above the spin-only value of 0.38 cm^3 mol^{-1} K for an LS Fe^{III} ion but in line with the commonly observed value of 0.50 cm^3 mol^{-1} K. Upon heating, the $\chi_M T$ curve overlays with that of cooling, indicating the absence of a hysteretic effect. Furthermore, after *in situ* heating at 400 K, the profile of the $\chi_M T$ curve remains similar, with a slightly higher transition temperature of $T_{1/2}$ = 259 K, again without any hysteretic effect being observed.

Complex **2** also demonstrated a complete SCO transition with a transition temperature $T_{1/2}$ of 189 K (Fig. 7b). The $\chi_M T$ value is 4.27 cm^3 mol^{-1} K at 300 K and 0.48 cm^3 mol^{-1} K at 5 K. No hysteresis loop was observed for this complex either. Unlike complex **1**, desolvation in complex **2** leads to a slight decrease in $T_{1/2}$ by about 10 K. Complex **3** exhibits a magnetic profile akin to complex **2**, with a transition temperature $T_{1/2}$ of 185 K (Fig. 7c). At 5 K, the $\chi_M T$ value of complex **3** is larger than that of complexes **1** and **2**, indicating a higher HS residue at low temperatures. While the magnetic behavior of complex **3** is similar to that of **1** and **2**, desolvation exerts a different impact on its magnetic properties. Notably, the SCO properties of the *in situ* heated sample of **3** were observed to be different for two different batches, either remaining in the HS state or exhibiting an incomplete hysteretic SCO transition at around 100 K (Fig. 7c). For example, for one batch of sample following *in situ* desolvation at 400 K in the SQUID VSM, the $\chi_M T$ curve gradually decreases from 4.47 cm^3 mol^{-1} K at 400 K to

4.06 cm^3 mol^{-1} K at 125 K, then drops quickly to 3.46 cm^3 mol^{-1} K at 70 K, and continues to decrease gradually to 3.07 cm^3 mol^{-1} K at 5 K. The SCO transition here is only partial, with an estimated HS Fe^{III} residue of 77% at 70 K ($\chi_M T = \gamma \times 4.38 + (1-\gamma) \times 0.38$, where γ is the proportion of HS state). Interestingly, a hysteresis loop of 19 K is observed, with the estimated $T_{1/2}\downarrow$ upon cooling and $T_{1/2}\uparrow$ upon heating being 97 K and 116 K, respectively. However, for another batch of the sample, the $\chi_M T$ curve after *in situ* desolvation remains almost constant from 400 to 5 K, indicating its HS state (Fig. 7c). Currently, the cause of this discrepancy is unclear, especially considering that the PXRD patterns of the two *in situ* desolvated samples after the magnetic measurement both align well with the simulated pattern based on the single crystal data of **3·0.6H$_2$O** (Fig. S3f†). We suspect that the slightly different desolvation degrees of different sample batches may be attributed for this observation.

As for complex **4**, it predominantly remains in the HS state above 5 K, with $\chi_M T$ values ranging from 4.50 cm^3 mol^{-1} K at 300 K to 3.95 cm^3 mol^{-1} K at 15 K (Fig. 7d). This is in line with the single crystal structure results, which showed the HS state Fe^{III} centers at both 100 and 300 K. However, a very minor dip in the $\chi_M T$ curve around 200 K can be observed, which is indicative of a subtle change in the magnetic properties. Upon *in situ* heating at 400 K, the desolvated complex **4** undergoes a gradual and complete SCO with a $T_{1/2}$ of 200 K. The PXRD patterns of the desolvated sample differ significantly from those of complex **4** (Fig. S18a†). Although the crystal structure of the desolvated complex **4** was not obtained, it was noted that the magnetic properties of complex **4** are highly sensitive to storage time under ambient conditions. As depicted in Fig. 7d, the magnetic properties were measured for samples stored at room temperature for varying periods (1 hour, 1 day, and 20 days). The proportion of the LS state at low temperature increases over time, with the SCO transition all occurring at around 200 K. With increasing aging time, the SCO towards the LS state becomes more complete, and after 20 days, the $\chi_M T$ curve approaches that of the *in situ* desolvated sample. Further analysis was conducted by TGA and PXRD on samples of different aging periods (Fig. S18†). The TGA results indicate a continuous decrease in the amount of residual lattice solvent. Concurrently, the PXRD patterns evolve from those characteristics of complex **4** to those of the fully desolvated sample. However, even after 20 days of aging, some CH_2Cl_2 solvent molecules remain in the sample. These findings highlight the sensitivity of complex **4** to environmental conditions and underscore the pivotal role of lattice solvent CH_2Cl_2 molecules on its SCO properties.

Differential scanning calorimetry (DSC) measurements

Differential scanning calorimetry (DSC) measurements on complexes **1–3**, conducted at a scan rate of 5 K min^{-1} (Fig. S19†) further elucidate their SCO behaviors. Complex **1** displays an exothermic/endothermic peak at 229/231 K during the cooling/heating process. The minor 2 K temperature difference is attributed to the measurement's temperature lag rather than a hysteretic effect. The calculated enthalpy and entropy changes are 6.94/6.78 kJ mol^{-1} and 30.28/29.34 J mol^{-1} K^{-1}, which are typical for Fe^{III} SCO compounds.[26,43] The entropy change exceeds the theoretical value for a pure spin transition (from $^2T_2$ to $^6A_1$, $\Delta S = R\ln(6/2) = 9.13$ J mol^{-1} K^{-1}), suggesting significant vibrational contributions[41] and also the order–disorder transition of NO_3^- anions. Complexes **2** and **3** exhibit DSC peaks at 192/190 K and 183/181 K on heating/cooling, closely aligning with their transition temperatures from magnetic property data. Their enthalpy and entropy changes are 1.61/1.62 kJ mol^{-1} and 8.39/8.51 J mol^{-1} K^{-1} for complex **2**, and 2.99/2.87 kJ mol^{-1} and 16.54/15.85 J mol^{-1} K^{-1} for complex **3**, respectively. These values are considerably smaller than those for complex **1**, with the entropy of complex **3** even lower than that for a pure SCO transition. This could be because the SCO occurs over a broad temperature range, and the calculation of enthalpy and entropy changes are based on only a part of this interval. Nevertheless, these values are consistent with previously reported data for similar Fe^{III}-qsal complexes.[33,44]

The DSC results for complexes **1–3** were employed to fit the $\chi_M T$ curves (Fig. 8) using a domain model with the following equation:[45]

$$\ln\frac{(1-\gamma_{HS})}{\gamma_{HS}} = \frac{n\Delta H}{RT} - \frac{n\Delta S}{R}$$

where n represents the number of molecules in an independent domain, γ_{HS} is the faction of the HS state, R is the ideal gas constant, ΔH is the enthalpy change, and ΔS is the entropy change. Generally, the larger n value is indicative of stronger cooperativity. For complexes **1** and **2**, the fitted n values are close to each other with values being around 9 and 10 (Table S12†), suggesting their comparable cooperativity due to their similar supramolecular structures. Complex **3**, on the other hand, exhibits an n value of 6, which is slightly lower than that of complexes **1** and **2**, indicating its slightly weaker cooperativity.

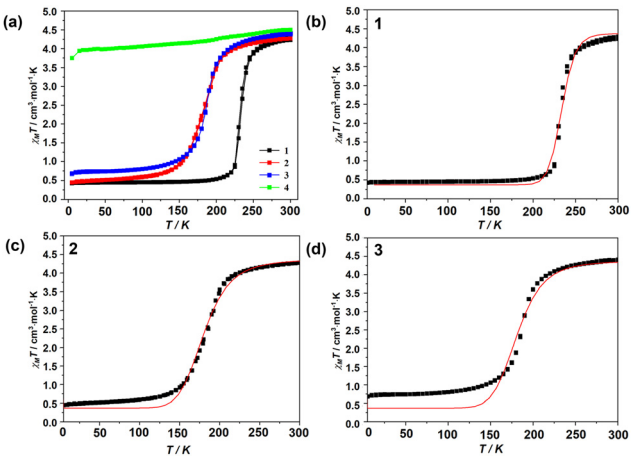

Fig. 8 (a) $\chi_M T$ *versus* T plots for **1–4** between 5 K and 300 K; and (b–d) fitting curves for complexes **1–3** using a domain model.

Magneto–structural relationship

The analysis of the magneto–structural relationships in complexes **1–4** could offer valuable insights for the further development of SCO materials. In general, the SCO properties of the materials are influenced by several factors, including counterions, lattice solvents, and the nature and positioning of substituent groups. These factors subtly regulate the ligand field and crystal packing, influencing intermolecular interactions and cooperativity. In complexes **1–4**, the anions and solvents in the crystal lattice significantly impact their SCO properties, with anion size being a key determinant of SCO temperatures (Fig. 8a). For the isostructural complexes **1** and **2**, which share similar crystal structures and the same lattice solvent molecules, the larger ClO_4^- anion in complex **1** compared to the NO_3^- anion in complex **2** leads to a higher transition temperature ($T_{1/2}$ = 230 K for **1** *vs.* $T_{1/2}$ = 189 K for **2**, Fig. 8a). This aligns with the general trend that smaller anions tend to stabilize the LS state with high $T_{1/2}$ values, while larger anions favor the HS state with lower $T_{1/2}$ values.[21,22] This effect is attributed to the looser packing structures and increased distortion of the ligands and metal coordination octahedra,[31] which can impede the SCO process.

The trend is also evident in complex **4**, which contains the largest NTf_2^- anion and remains in the HS state. However, complex **3**, with an OTf^- anion larger than ClO_4^- in complex **2**, exhibits a similar $T_{1/2}$ value as complex **2**. This discrepancy is likely due to the influence of the solvent. As previously discussed, the presence of MeOH molecules in **3** results in more hydrogen bonds compared to complex **2**, which appears to strengthen the intermolecular interactions (Tables S7 and S8†). This enhanced interaction seems to counterbalance the effect of larger OTf^- anion, leading to their similar transition temperatures.

While desolvation induces minor modifications in the SCO properties of complexes **1** and **2**, its impact is more pronounced in complexes **3** and **4**, resulting in significant changes to their SCO behaviors. For complex **3**, desolvation results in either a HS state or an incomplete hysteretic transition with a low transition temperature for different sample batches. As can be seen from its crystal structure, the desolvated form, **3·0.6H$_2$O**, shows weaker intermolecular interactions, which may be attributed for the looser packing and reduced transition temperature. Complex **4** also exemplifies the pivotal role of lattice solvent molecules in SCO behavior. Magnetic measurements on samples of varying aging times have demonstrated that while complex **4** remains in an HS state in the temperature range of 5 to 300 K, the removal of CH_2Cl_2 molecules induces an SCO transition. This scenario contrasts with that of complex **3**. Although the precise impact of the interactions involving CH_2Cl_2 on SCO is not fully understood, the removal of these weakly interacting molecules leads to tighter packing of the structure, potentially driving the SCO transition.

Finally, as the main purpose of this study, the Br substituent on the Hqnal ligand plays a significant role in the structures and SCO properties of the studied complexes. For comparison, the reported Fe^{III} SCO complexes featuring the Hqnal ligand are listed in Table S13.† However, comparing these complexes with our Hqnal-5-Br$_q$ compounds does not yield a clear conclusion regarding the impact of bromine substation on SCO characteristics. For example, among complexes with identical anions, $[Fe(qnal)_2]CF_3SO_3$·MeOH exhibits a lower $T_{1/2}$ than our compound **3**, while $[Fe(qnal)_2]NO_3$, which remains in the LS state below 300 K, has a significantly higher $T_{1/2}$ than our compound **1**. Therefore, while the introduction of bromine is confirmed to influence SCO behaviors, including transition temperatures and cooperativity, the complexity of solid-state SCO, influenced by factors such as anions, solvents, and substituents, makes it challenging to pinpoint the precise effect on the properties. Direct comparisons of transition temperatures and cooperativity among similar ligands with different substituents in the solid state may not be explanatory. For a clearer understanding, it would be ideal to examine a series of isostructural complexes that maintain the same anions and solvents, with the only variable being the substituent in question. Additionally, investigating SCO behaviors in solution could provide valuable insights by eliminating the influence of solid-state packing effects. Such studies are scarce in the literature for Fe^{III} SCO complexes with qsal and qnal type ligands, and they are beyond the scope of this manuscript. Nevertheless, it is evident that the introduction of a substituent will invariably lead to the development of new SCO materials with distinct structures and magnetic properties.

Conclusions

In conclusion, we reported here the synthesis and thorough characterization of a new quinoline-substituted ligand, Hqnal-5-Br$_q$, and a series of Fe^{III} SCO complexes $[Fe(qnal\text{-}5\text{-}Br_q)_2]$A·solvent (A = NO_3^- **1**, ClO_4^- **2**, OTf^- **3**, and NTf_2^- **4**) based on this ligand. Despite the different anions, these complexes all feature similar 1D $[Fe(qnal\text{-}5\text{-}Br_q)_2]^+$ cation chains primarily formed by the π···π interactions between the qnal-5-Br$_q$ ligands. Magnetic studies revealed that complexes **1–3** undergo abrupt SCO, while complex **4** remains in the high-spin state above 5 K. The transition temperatures of these complexes tend to decrease with the increasing size of the anions. Furthermore, the effect of solvents on SCO properties was examined through magnetic measurements of the desolvated samples. Desolvation marginally affects complexes **1** and **2** but significantly alters the SCO profiles of complexes **3** and **4**. Notably, the desolvation of complex **3** proceeds *via* a crystal-to-crystal transformation to obtain **3·0.6H$_2$O**, whereas it occurs in a more gradual process for complex **4**, with the residue solvent content varying with the aging period. These results reported here highlight the significant role of the substituent on the Hqnal ligands on the development of new SCO materials. More results from our group will be reported shortly.

Data availability

The data published in this contribution are available in the ESI.†

Crystallographic data have been deposited with the Cambridge Crystal Structure Database (CCDC).

Conflicts of interest

There are no conflicts to declare.

Acknowledgements

This work was supported by the National Natural Science Foundation of China (22273036 and 21973039).

References

1 P. Gütlich and H. A. Goodwin, *Top. Curr. Chem.*, 2004, **233**, 1–47.
2 P. Gütlich, A. B. Gaspar and Y. Garcia, *Beilstein J. Org. Chem.*, 2013, **9**, 342–391.
3 D. Tesfaye, W. Linert, M. Gebrezgiabher, Y. Bayeh, F. Elemo, T. Sani, N. Kalarikkal and M. Thomas, *Molecules*, 2023, **28**, 1012.
4 D. J. Harding, P. Harding and W. Phonsri, *Coord. Chem. Rev.*, 2016, **313**, 38–61.
5 P. Guionneau, *Dalton Trans.*, 2014, **43**, 382–393.
6 L. J. K. Cook, H. J. Shepherd, T. P. Comyn, C. Baldé, O. Cespedes, G. Chastanet and M. A. Halcrow, *Chem. – Eur. J.*, 2015, **21**, 4805–4816.
7 M. Nakaya, R. Ohtani, L. F. Lindoy and S. Hayami, *Inorg. Chem. Front.*, 2021, **8**, 484–498.
8 Y. Z. Li, Y. Y. Wu, Y. Li, H. J. Wang, A. Sulaiman, K. Mohammad Javed, C. Y. Zhang, W. Li and H. X. Bu, *CCS Chem.*, 2023, **5**, 412–422.
9 R. Díaz-Torres, G. Chastanet, E. Collet, E. Trzop, P. Harding and D. J. Harding, *Chem. Sci.*, 2023, **14**, 7185–7191.
10 B. J. C. Vieira, L. C. J. Pereira, V. D. Gama, I. C. Santos, A. C. Cerdeira and J. C. Waerenborgh, *Magnetochemistry*, 2022, **8**, 19.
11 R. Díaz-Torres, S. Gómez-Coca, E. Ruiz, P. Harding and D. J. Harding, *Dalton Trans.*, 2023, **52**, 18148–18157.
12 S. Hayami, Z. Z. Gu, H. Yoshiki, A. Fujishima and O. Sato, *J. Am. Chem. Soc.*, 2001, **123**, 11644–11650.
13 S. Hayami, T. Kawahara, G. Juhasz, K. Kawamura, K. Uehashi, O. Sato and Y. Maeda, *J. Radioanal. Nucl. Chem.*, 2003, **255**, 443–447.
14 J. C. Dias, B. Vieira, I. C. Santos, L. C. J. Pereira and V. da Gama, *Inorg. Chim. Acta*, 2009, **362**, 2076–2079.
15 D. J. Harding, D. Sertphon, P. Harding, K. S. Murray, B. Moubaraki, J. D. Cashion and H. Adams, *Chem. – Eur. J.*, 2013, **19**, 1082–1090.
16 D. Sertphon, D. J. Harding, P. Harding, K. S. Murray, B. Moubaraki and H. Adams, *Aust. J. Chem.*, 2014, **67**, 1574–1580.
17 D. Sertphon, D. J. Harding, P. Harding, K. S. Murray, B. Moubaraki, H. Adams, A. Alkas and S. G. Telfer, *Eur. J. Inorg. Chem.*, 2016, **3**, 432–438.
18 R. Díaz-Torres, W. Phonsri, K. S. Murray, P. Harding and D. J. Harding, *Cryst. Growth Des.*, 2022, **22**, 1543–1547.
19 R. Díaz-Torres, T. Boonprab, S. Gómez-Coca, E. Ruiz, G. Chastanet, P. Harding and D. J. Harding, *Inorg. Chem. Front.*, 2022, **9**, 5317–5326.
20 W. Phonsri, P. Harding, L. J. Liu, S. G. Telfer, K. S. Murray, B. Moubaraki, T. M. Ross, G. N. L. Jameson and D. J. Harding, *Chem. Sci.*, 2017, **8**, 3949–3959.
21 H. J. Sheng, C. C. Xia, X. Y. Zhang, C. C. Zhang, W. J. Ji, Y. Zhao and X. Y. Wang, *Inorg. Chem.*, 2022, **61**, 12726–12735.
22 R. Díaz-Torres, W. Phonsri, K. S. Murray, L. J. Liu, M. Ahmed, S. M. Neville, P. Harding and D. J. Harding, *Inorg. Chem.*, 2020, **59**, 13784–13791.
23 A. Tsukiashi, M. Nakaya, F. Kobayashi, R. Ohtani, M. Nakamura, J. M. Harrowfield, Y. Kim and S. Hayami, *Inorg. Chem.*, 2018, **57**, 2834–2842.
24 K. Takahashi, H. B. Cui, Y. Okano, H. Kobayashi, H. Mori, H. Tajima, Y. Einaga and O. Sato, *J. Am. Chem. Soc.*, 2008, **130**, 6688–6689.
25 M. Nakaya, K. Shimayama, K. Takami, K. Hirata, A. S. Alao, M. Nakamura, L. F. Lindoy and S. Hayami, *Chem. Lett.*, 2014, **43**, 1058–1060.
26 F. L. Chen, Y. C. Sun, X. L. Liu, G. Li, C. C. Zhang, B. H. Gao, Y. Zhao and X. Y. Wang, *Inorg. Chem.*, 2024, **63**, 8750–8763.
27 G. M. Sheldrick, *CELL_NOW*, Georg-August-Universität, Göttingen, Germany, 2008.
28 G. M. Sheldrick, *TWINABS 2012/1*, Bruker, Madison, Wisconsin, USA, 2012.
29 G. M. Sheldrick, *Acta Crystallogr., Sect. A: Fundam. Crystallogr.*, 2008, **64**, 112–122.
30 G. M. Sheldrick, SHELXT - Integrated space-group and crystal-structure determination, *Acta Crystallogr., Sect. A: Found. Adv.*, 2015, **71**, 3–8.
31 O. V. Dolomanov, L. J. Bourhis, R. J. Gildea, J. A. K. Howard and H. Puschmann, *J. Appl. Crystallogr.*, 2009, **42**, 339–341.
32 J. Sirirak, W. Phonsri, D. J. Harding, P. Harding, P. Phommon, W. Chaoprasa, R. M. Hendry, T. M. Roseveare and H. Adams, *J. Mol. Struct.*, 2013, **1036**, 439–446.
33 S. E. Lazaro, A. Alkas, S. J. Lee, S. G. Telfer, K. S. Murray, W. Phonsri, P. Harding and D. J. Harding, *Dalton Trans.*, 2019, **48**, 15515–15520.
34 U. Habarakada, T. Boonprab, P. Harding, K. S. Murray, W. Phonsri, S. M. Neville, M. Ahmed and D. J. Harding, *Cryst. Growth Des.*, 2022, **22**, 4895–4905.
35 A. R. Jeong, S. R. Park, J. W. Shin, J. Kim, R. Tokunaga, S. Hayami and K. S. Min, *Dalton Trans.*, 2024, **53**, 6809–6817.

36 R. T. Marques, L. P. Ferreira, C. S. B. Gomes, C. S. D. Lopes, C. E. S. Bernardes, N. K. Sarangi, T. E. Keyes and P. N. Martinho, *Cryst. Growth Des.*, 2023, **23**, 3222–3229.
37 D. J. Harding, W. Phonsri, P. Harding, I. A. Gass, K. S. Murray, B. Moubaraki, J. D. Cashion, L. J. Liu and S. G. Telfer, *Chem. Commun.*, 2013, **49**, 6340–6342.
38 K. Fukuroi, K. Takahashi, T. Mochida, T. Sakurai, H. Ohta, T. Yamamoto, Y. Einaga and H. Mori, *Angew. Chem., Int. Ed.*, 2014, **53**, 1983–1986.
39 W. Phonsri, C. G. Davies, G. N. L. Jameson, B. Moubaraki and K. S. Murray, *Chem. – Eur. J.*, 2016, **22**, 1322–1333.
40 K. Tomono, Y. Tsun, M. Llunell, D. Casanova, J. Cirera, P. Alemany and S. Alvarez, *SHAPE, version 2.1*, Universitat de Barcelona, Barcelona, Spain, 2013.
41 N. Phukkaphan, D. L. Cruickshank, K. S. Murray, W. Phonsri, P. Harding and D. J. Harding, *Chem. Commun.*, 2017, **53**, 9801–9804.
42 M. J. Turner, J. J. McKinnon, S. K. Wolff, D. J. Grimwood, P. R. Spackman, D. Jayatilaka and M. A. Spackman, *CrystalExplorer17*, University of Western Australia, Perth, Australia, 2017.
43 S. Murata, K. Takahashi, T. Mochida, T. Sakurai, H. Ohta, T. Yamamoto and Y. Einaga, *Dalton Trans.*, 2017, **46**, 5786–5789.
44 D. J. Harding, W. Phonsri, P. Harding, K. S. Murray, B. Moubaraki and G. N. L. Jameson, *Dalton Trans.*, 2015, **44**, 15079–15082.
45 O. Kahn, *Molecular Magnetism*, VCH, Weinheim, Germany, 1993, pp. 66–67.